

Ozone in the boreal forest in the Alberta oil sands region

Xuanyi Zhang¹, Mark Gordon¹, Paul A. Makar², Timothy Jiang^{1*}, Jonathan Davies², David Tarasick²

¹Earth and Space Science, York University, Toronto, M3J 1P3, Canada

²Air Quality Research Department, Environment and Climate Change Canada, Toronto, M3H 5T4, Canada

5 *Now at School of Environmental Sciences, Guelph University, Guelph, N1G 2W1, Canada

Correspondence to: Mark Gordon (mgordon@yorku.ca)

Abstract. Measurements of ozone were made using an instrumented tower and a tethered sonde located in a forested region surrounded by oil sands production facilities in the Athabasca Oil Sands Region (AOSR). Our observations and modelling show that the concentration of ozone was modified by vertical mixing, photochemical reactions, and surface deposition. Measurements on the tower demonstrated that when winds are from the direction of anthropogenic emissions from oil sand extraction and processing facilities, the ozone mixing ratio in the forest can be as much as 10 ppb lower than when winds are from the direction of undisturbed forest. This finding is supported by previous studies which suggest that ozone is destroyed by reaction with NO_x from oil sands extraction operations (as well as NO resulting from photolysis of NO₂). Vertical gradients of ozone mixing ratio with height were observed using instruments on a tethered balloon (up to a height of 300 m) as well as a pulley system and 2-point gradients within the canopy. Strong gradients (ozone increasing with height between 0.2 and 0.4 ppb m⁻¹) were measured in the canopy overnight, while daytime gradients were weaker and highly variable. A 1D canopy model was used to simulate the afternoon in-canopy gradient with reduced mixing overnight (suggesting high stability within the canopy), and an ozone deposition velocity of 0.2 cm s⁻¹. Sensitivity simulations using the model suggest the local NO concentration profile and coefficients of vertical diffusivity have a significant influence on the O₃ concentrations and profiles in the region.

1 Introduction

Canada's largest oil sands deposits areas are found in the Athabasca Oil Sands Region (AOSR) of northern Alberta. The increasing oil sands production has led to increased environmental concern for the nearby forest ecosystem (Li et al., 2017). The processes of oil and gas extraction from oil sands include surface mining to turn surface oil sands into crude oil, well injection to pump deeper bitumen onto the surface, extraction of bitumen from oil sands with the water-based process and the upgrading of bitumen into hydrocarbon streams (Natural Resources Canada, 2016).

Ozone is a photochemical pollutant in the troposphere. It is produced there by the photochemical oxidation of carbon monoxide, methane, and non-methane volatile organic compounds in the presence of nitric oxide (NO) and nitrogen dioxide (NO₂). All these species are emitted from activities in the oil sands.

30 In the AOSR, Cho et al. (2017) observed no statistically significant increase in long-term ozone measurements over the 1998 to 2012 period, despite an 8% annual increase in NO_x emissions. The lack of a local ozone increase was attributed to NO_x from local emissions, which results in titration of ambient ozone. Similarly, Aggarwal et al. (2018) measured ozone levels in the Alberta oil sands region (between the ground and a height of 1.8 km) which were lower than or equal to the background ozone mixing ratio, which is also attributed to NO titration. The absence of enhanced ozone downwind of industry was associated with air temperatures less than 20°C and vertical mixing of polluted and clear background air.

The motivation for this study is to a) determine how pollutant emissions associated with oil sands extraction modify ozone concentration in the surrounding forest, and b) investigate how the forest affects ozone deposition. A boreal forest site was chosen that is surrounded by oil sands processing facilities including those operated by Syncrude, Suncor, Canadian Natural Resources Limited (CNRL), as well as other facilities. Since exposure to ozone reduces photosynthesis, growth, and other plant functions (Felzer et al., 2007), we investigate what effect the elevated pollution levels of the AOSR have on the surrounding boreal forest and to determine the rate of ozone uptake to the forest.

Finco et al. (2018) analyzed ozone deposition in a deciduous forest (in a highly polluted region in Italy) based on measurements from the understory up to above the canopy. They found that ozone deposition increased with height within the canopy. Ozone fluxes were much higher at the canopy level within the foliage (24 m) compared to the above canopy region, and stomatal deposition was the main ozone removal process (with less than 20% removed by chemical reaction with NO and by non-stomatal deposition). High stomatal conductance leads to high stomatal uptake of ozone. The peak of stomatal conductance occurs when the ambient air is warm and humid (Ducker et al., 2018). Stomatal closure occurs in the nighttime, and then non-stomatal deposition processes become the main ozone deposition process (Pilegaard, 2001). The dominant chemical loss process is NO reaction with O₃ below the canopy (Kaplan et al., 1988). There are also monodirectional fluxes of NO and NO₂, with NO emitted from the soil and NO₂ deposited to the ground (Finco et al., 2018). However, Wolfe et al. (2011) have demonstrated that chemical loss due to VOCs can also be significant.

Rannik et al. (2012) measured ozone deposition to a boreal forest using eddy covariance over a 10-year period. They determined that the ozone deposition velocity (v_d) was 0.4 cm s⁻¹ during the peak growing season. Multivariate analysis demonstrated that v_d was correlated with photosynthetic capacity of the canopy, vapour pressure deficit, photosynthetically active radiation, and monoterpene concentration. Wu et al. (2016) determined v_d at a mixed boreal-temperate transition forest over a 5-year period using a gradient approach. The highest monthly mean of ozone deposition velocity was 0.68 cm s⁻¹ and the 5-year average and median were 0.35 and 0.27 cm s⁻¹ respectively. The average ozone deposition velocity in the summer was near 0.4 cm s⁻¹ at night, increased to 1 cm s⁻¹ in the morning, and then decreased steadily through the day back to the nighttime value.

60 Makar et al. (2017), herein M17, demonstrated that the turbulence and shading effects of forests on ozone mixing and chemistry have been poorly modeled in global and regional air-quality models. The changes in turbulence within the canopy (due to friction, wind shear, and momentum absorption) modify how ozone and reactive species (such as NO) are mixed into and out of the canopy. Regional chemical transport models by default usually do not explicitly include the shading of forest

canopies in photolysis calculations; this plus the reduced turbulence within the canopy create a darker and more stable environment than is usually simulated in atmospheric models. Improving how canopy shading and turbulence are modeled changes the rates of photochemical reactions occurring in the canopy, typically leading to more near-surface ozone titration. Including both these effects in a regional air-quality model accounted for 97% of the previous positive bias in forested regions. Approximately one-third of this improvement was attributed to the shading effect, while two-thirds was due to the change in turbulence parameterization. Hence, any accurate modeling of ozone within a forest must include both turbulence and shading effects.

A recent review of ozone deposition by Clifton et al. (2020) highlights the need for both short-term field intensives and long-term deposition sites. The review synthesizes the current knowledge of deposition pathways, including stomatal, non-stomatal, and soil uptake and in-canopy chemistry. While our study is not able to distinguish these various pathways, the motivation is to investigate how oil sand extraction and processing affects ozone mixing ratios and deposition. This study focusses on ozone deposition analysis using vertical ozone mixing ratio gradients within and above a jack pine forest canopy in a forest region surrounded by oil sand production facilities. Ozone mixing ratio was measured above and within the forest canopy, as well as ultraviolet radiation (UV), photosynthetically active radiation (PAR), and meteorological variables. Gradient and mixing ratio measurements are compared with a 1D canopy model with various deposition schemes using a “big leaf” approach, which assumes a deposition flux at the lowest model layer. This paper is a companion paper to Jiang et al. (2022) and Gordon et al. (2022) which respectively investigate aerosol and SO₂ deposition at this site.

2 Methods

2.1 Site Location and Instrumentation

The study site is characterized by a surrounding homogeneous jack pine forest with flat topography, in turn surrounded by oil processing and extraction facilities. This selected forest area (Fig. 1) is far from cities, and the nearest habitation (Fort McKay) is about 11 km to the Northwest of the study site, with a population of only 700. The nearest town of Fort McMurray is approximately 45 km south of the site. The nearest highway is approximately 650 m south of the study site. The traffic on this highway is light, with usually 1 or 2 transport trailers or large trucks per minute. Thus, the effect from the town and the highway can be assumed to be negligible for this study and the pollution detected in the forest was mainly from the surrounding oil sands processing facility plumes.

In July 2017, the York Athabasca Jack Pine (YAJP) tower was installed at the study site at 57.1225 N 111.4264 W. The tower is 29 m high, and the canopy is about 19 m high (with the tallest trees ranging from 16 m to 21 m in height). In the 2017 field study, an ozone analyzer (Model 205, 2B Tech) and a UV sensor (CUV5, Kipp & Zonen) were mounted on a sub-canopy tower pulley system to measure ozone and UV profiles between the ground and a height of 16 m. A table platform was used on the pulley (with ropes attached at each corner) to ensure the UV sensor remained level. The data were collected for periods of 5-min intervals at 5-m height intervals after ensuring the sensors were level and not moving.

During a 2018 summer intensive field campaign (9 to 17 June) two ozone monitors (Model 205, 2B Tech.) were mounted on the tower at heights of 25 m and 2 m. Ozone and SO₂ analyzers (49i and 43i, Thermo Scientific) sampled from a height of 2 m. A generator was used to power the instruments during the field intensives, which was placed 100 m from the tower in the northeast direction (at a wind direction of 40°), since regional winds are typically not from this direction. For 3 days during this study, a Vaisala Tethered-Balloon system (Vaisala DigiCORA) was used for short-term ozone profile measurements. The balloon lifted one tethersonde (TTS111, Vaisala) and an ozonesonde (Smit et al., 2007) with an Arduino data logger. Calibration and uncertainty of the ozone instruments is discussed in the following section.

After the 2018 field experiment, a solar-powered ozone monitor (Model 405, 2B) was left on the tower at a height near 19 m. This ran continuously until mid-July, and then intermittently until mid-August, after which there was inadequate sunlight for the solar-power system. In March 2019, two solar-powered ozone monitors (Model 405, 2B) were left on the tower at heights of 2 m and 25 m for long-term monitoring. The monitors were activated 4 times per day (02:00, 08:00, 14:00, and 20:00 local) for one hour duration. The sampling frequency during these time periods was 0.25 Hz. To allow the instrument to equilibrate after each cold start, the measurement for each period was taken as the average value of the last 15-minutes of measurement in each hour. The uncertainty associated with this technique is discussed in the following section. These monitors remained operational until late June 2019.

During August 2021, there was a third summer intensive study at the tower. No ozone measurements were made during this field study, but SO₂ measurements (43i, Thermo Scientific and AF22e, Envea) at ground level and a height of 30 m and size-resolved sub-micron aerosol measurements (UHSAS, DMT) helped to further identify wind sectors bringing polluted air to the site. The SO₂ and aerosols measurements are discussed in our companion papers Gordon et al. (2022) and Jiang et al. (2022) respectively.

Permanent instruments on the YAJP tower (solar powered) used for the following analysis include sonic anemometers (ATI Inc.) at heights of 29 m and 5.5 m, photosynthetically active radiation (PAR, LI-190, Licor Inc) measured at heights of 29 m, 15.9 m, and 2 m, and a gas analyzer (CO₂/H₂O, LI-7500, Licor Inc) at a height of 29 m. These instruments were factory calibrated and data were quality controlled through visual inspection of the time series, resulting in rejection of less than 0.1% of the data.

The Wood Buffalo Environmental Association (WBEA) operates a meteorological tower identified as “1004” which is approximately 540 m south of the YAJP tower. The 1004 tower measures hourly values of: temperature, relative humidity (RH) and winds at heights of 2, 16, 21, and 29 m; PAR at heights of 2, 16, and 21 m; and atmospheric pressure (at 2 m).

2.2 Ozone Instrument Uncertainty

The 49i analyzer was laboratory-calibrated prior to the study (a 7-point calibration up to 120 ppb with $R^2 = 0.997$). The standard deviation in the 5-second measurement during calibration was 1.9 ppb. All Model 205 and ozonesonde monitors were calibrated in the field against the 49i analyzer by running the instruments side-by-side for 9 consecutive days period (at a 0.5 Hz frequency) prior to the long-term averaging periods. The ozone mixing ratio varied from near 1.3 ppb to 38 ppb

during this period. The root-mean-square errors (RMSE) against the calibrated 49i were less than 2 ppb (at 0.5 Hz). The 2B
130 Ozone Monitor specifications (2B Specifications) give a drift value of $< 1 \text{ ppb day}^{-1}$ and $< 3 \text{ ppb year}^{-1}$. Over the 9-day
period, the RMSE (at 0.5 Hz) showed no discernable trend with time. A least-squares fit of RMSE with time give a trend of
 $0.004 \text{ ppb day}^{-1}$ (which is not significantly different from zero at a 95% confidence level (C.I.)). Hence, we assume minimal
drift during the 3-month measurement period. Water vapour interference is assumed to be minimal since the 2B analyzers
135 have a built-in dryer and heater to eliminate water vapour interference and temperature effects (2B Specifications), and the
inlet tubing is only 10 cm in length.

During the long-term, 2019 measurements, when the monitors were activated 4 times per day for one-hour durations, the
monitors were allowed to stabilize for 45 minutes and only the last 15-minutes of measurements were used. The
manufacturer specifies (2B Specification) a 20-minute warm-up period. The stabilization of the instrument is demonstrated
in the supporting information (Fig. S1) from the measured data, indicating full stabilization may require approximately 35
140 minutes. A truncated mean is calculated from the last 15 minutes, with outliers more than 3 standard deviations from the
mean removed (resulting is removal of less than 0.5% of data). The average standard deviation in this 15-minute interval is
1.8 ppb, which gives a 95% C.I. of $\pm 0.24 \text{ ppb}$ (for each 15-minute average).

2.3 Ozone Modeling

To model photochemical processes, diffusion, and deposition in the canopy, we use a one-dimensional (1D) canopy model
145 created by Makar et al. (1999). The model has 1001 levels in the vertical direction, and each level has 1-m spacing. The
model uses 30-minute interval input data. It includes 268 chemical reactions associated with 79 output species. In the 1-D
canopy model, the rate of change of each chemical species mixing ratio (C) at each model level is calculated due to their
emissions (E), chemical reactions (f) and diffusion (Eq. 1) at each layer. In Equation 1, subscript m represents different
chemical species, subscript n represents the vertical layer, and K is the eddy diffusivity.

$$150 \quad \frac{\partial C_{mn}}{\partial t} = E_{mn} + f_{mn} + \frac{\partial}{\partial z} \left(K(z_n) \frac{\partial C_{mn}}{\partial z} \right), \quad (1)$$

Further modifications were made to the model outlined in Stroud et al. (2005) and Gordon et al. (2014) to include
sesquiterpenes, modify the diffusion code, and include surface deposition. This model version uses operator splitting in each
minute. First, each species diffuses for 30 seconds using a Crank-Nicholson numerical scheme to solve the diffusion term in
Eq. 1. This is followed by 1 minute of uptake or emissions (E) and chemistry (f). Then the species diffuse for another 30
155 seconds. This process is repeated 30 times for each 30-min time step.

Model input variables are updated every 30 minutes. The model uses input data of pressure, PAR, and RH at a single height.
Temperature and NO are input for the lowest 50 levels with 1 m spacing and the turbulent diffusion coefficient (K) is input
for all 1001 levels at 1 m spacing. Temperature profiles were linearly interpolated using the 2, 16, 21, and 29 m
measurements from the 1004 tower. Initially, the temperature was set as constant above a height of 29 m, but test runs
160 demonstrated improvement by assuming a dry adiabatic lapse rate (0.0098 K m^{-1}) above this height. As a sensitivity test, we

run versions of the model with constant temperature above 29 m and with a dry adiabatic lapse rate above this height (Section 3.5). Pressure, PAR, and relative humidity are required as model inputs at the canopy height. These variables were measured using the gas analyzer (LI-7500) and PAR (LI-190) sensors. Based on the availability of driving data, we ran the model for 6.5 days from 18:00 (local time) on 20 Jun to 06:00 on 27 Jun 2018. NO was not measured at the site, and the choice of NO inputs as a model boundary condition is discussed in the following section. The measured ozone mixing ratio at a height of 22 m was used to initiate the model. The first 12 hours of simulation are not used in this modeling analysis to allow for model spin-up, which gives 6 days of measurement-to-model comparison.

Above the canopy height, the diffusion coefficient, $K(z_n)$, was extracted from the GEM-MACH model for the simulated time period at the 16 GEM-MACH levels (z_n) ranging from approximately 21 m and 1040 m (a.s.l.) in 1-hour intervals. Half-hourly K values, required as inputs for the 1D canopy model, were linearly interpolated from the hourly values. The diffusion coefficient is calculated in GEM-MACH as (Mailhot and Benoit, 1982)

$$K = 0.516 \kappa z_m \frac{\sqrt{e}}{\phi} \quad (2)$$

where $\kappa = 0.4$, e is the turbulent kinetic energy, and ϕ is a stability parameter. Since e was measured at the YAJP tower at a height of $z_m = 29$ m, the GEM-MACH profiles are corrected to this value using a time-varying correction ratio (applied equally to all heights). Hence, the GEM-MACH K vertical profile shape is preserved, but the modeled values were adjusted to observations. The stability factor and Obukhov length are determined following Garratt (1994) as

$$\phi = \begin{cases} 0.74 \left(1 - 9 \frac{z_m}{L}\right)^{-1/2} & \frac{z_m}{L} < 0 \\ 0.74 + 4.7 \frac{z_m}{L} & \frac{z_m}{L} \geq 0 \end{cases}, \quad (3a)$$

$$L = -\frac{u_*^3 T}{\kappa g \overline{w'T'}}, \quad (3b)$$

using the friction velocity (u_*), temperature (T), and heat flux ($\overline{w'T'}$) measured at a height of $z_m = 29$ m on the YAJP tower (and $g = 9.8 \text{ m s}^{-2}$).

Within the canopy, K is modeled following the parameterization outlined in M17, where a generic within-canopy profile of K is imposed and is normalized relative to an above-canopy K value, with the intent of capturing the typical “shelf” in the decrease of K with decreasing height seen in multiple forest observations (e.g. Raupach, 1996). The M17 parameterization is normalized to the GEM-MACH model value of $K(z_l)$ at the lowest layer height, z_l , which was approximately 50 m in M17. Here, we normalize to the lowest model layer height in the updated version of GEM-MACH, which is $z_l = 23$ m. Since this is only slightly higher than the canopy height of $h_c = 19$ m and the effect of canopy turbulence has been shown to extend to twice the canopy height (Mölder et al., 1999), we also normalize to the height of the second lowest model layer $z_l = 42$ m (from M17) as a sensitivity test (Section 3.5). When normalized to the GEM-MACH $K(z_l)$, the M17 parameterization of K within the canopy is only a function of stability (h_c/L).

190 Ozone deposition was modeled with a “big leaf” assumption, where deposition is entirely attributed to the surface ($z = 0$) layer and uptake to the canopy (such as deposition to pine-needle surface or stomata) is ignored. This is modeled as a surface-flux boundary condition in the diffusion solver. While a vertical distribution of uptake (or locating the “big leaf” at a specified height above the surface) would be more realistic, this would require placement of the ozone uptake in the emission and chemistry operator step (as opposed to the diffusion operator).

195 Since ozone is depleted in the 1D model through deposition and chemistry, it must be replaced at the upper boundary of the model (1001 m). This is done by holding the concentration at the highest model layer constant as an upper boundary condition. This value is estimated based on a measured peak daily ozone near 50 ppb (at a height of 22 m) and a continued increase of ozone with height of 0.01 ppb m^{-1} (based on measurements shown in Sections 3.2 and 3.3), giving a constant upper-layer ozone value of 60 ppb. The choice of model height (1001 m) was determined by inspecting vertical ozone
200 profiles from ozonesonde launches at Bratt’s Lake (Astitha et al., 2018), which is located approximately 500 km SSW of the oil sands region. The aggregate vertical profile shows a consistently steep gradient between the surface and a height of 1 km (approximately 20 ppb km^{-1}) and a much weaker gradient between 1 km and 2 km ($< 3 \text{ ppb km}^{-1}$). Based on this, we choose a 1 km upper boundary of the model and ozone is held constant at this height. Sensitivity to both the assumed constant value and the choice of model height (1001 m) are tested in Section 3.5.

205 Canopy shading is accounted for in the model with PAR attenuation through the canopy as (Makar et al., 1999)

$$I_i = I_0 \exp(-k \sum L_i / \cos \theta), \quad (4)$$

where I_i is PAR at each level i , I_0 is the above canopy PAR, $\sum L_i$ is the leaf-area index (LAI), summed from the canopy top to level i within the canopy, k is an extinction coefficient, and θ is the solar zenith angle. The measured PAR above the canopy and at the surface suggests a value of $k = 0.68$, which is close to the value of 0.70 used by Stroud et al. (2005) for a
210 pine plantation in North Carolina, but much higher than the value of 0.31 for jack pine determined from the classification scheme described in M17 (with $k = G\Omega = 0.5 \times 0.62$). Sensitivity of the model to this parameter is also tested in Section 3.5. The canopy LAI profile was measured by analyzing fish-eye lens video at various heights (mounted on the pulley system) with the Gap Light Analyzer (GLA) software (Frazer et al., 1999). The LAI profile determined for the forest is shown in Figure 2. The total LAI was measured using ground level images from the area in the vicinity of the tower. This gives a total
215 LAI of 1.17 at the site. We compare this measured value to LAI from MODIS-derived seasonal LAI maps at 2.5 km resolution (Zhang et al, 2021). The site location is near the edge of two 2.5 km grid cells (see supporting Figure S2) with values of 1.09 and 1.27 in January and 1.89 and 2.23 in July. While the site is in an area dominated by jack pines, the surrounding area (within a few kilometers) also includes black spruce dominated stands and sphagnum dominated muskeg. The seasonal variation of the MODIS-derived values suggests deciduous trees in the surrounding area. To investigate a
220 possible underestimation of the surrounding representative LAI, we ran two sensitivity tests with LAI values of 2 and 3.5. While the modified LAI affects the light penetration into the canopy, it does not affect the turbulence profile, as the M17 parameterization of K does not include dependence on LAI.

As is outlined in Makar et al. (1999), the model includes forest emissions of isoprene and monoterpenes following Guenther et al. (1993). Here we use base emission rates of $8 \mu\text{g g}^{-1} \text{h}^{-1}$ for isoprene and $2.4 \mu\text{g g}^{-1} \text{h}^{-1}$ for monoterpene from Guenther et al. (1995) for boreal conifers (which includes both the local jack pine forest and surrounding black spruce). Sesquiterpene emission rates are set to 1/3 the monoterpene emission rates following Stroud et al. (2005). We test the sensitivity to these emission rates in Section 3.5.

2.4 NO Simulations in the Model

Since NO is an advected species, carried to the site from upwind emissions, it is prescribed as an input variable at each time-step and is not modeled as a time-varying species according to Equation 1. Initial model runs demonstrated that the model's ability to predict ozone is strongly dependent on the choice of NO used as a boundary condition. Due to this sensitivity, we consider and compare several different NO input scenarios to determine the effect on ozone mixing ratios and gradients. These scenarios comprise of NO modeled from GEM-MACH output, NO as a function of wind direction, an optimized constant NO value, elevated NO near the surface, and finally a diurnal switching between daytime and nighttime NO values. Firstly, surface-level NO mixing ratios were extracted from the GEM-MACH model (M17) in 1-hour intervals (which were linearly interpolated to 30-min values). The 1D canopy model assumes a constant NO mixing ratio with height. Initial test runs showed that using the GEM-MACH NO values, the timing of plumes arriving at the YAJP tower is mis-aligned relative to measurements. The proximity of nearby stack sources (within ~ 16 km) means that small changes in wind direction can determine whether the YAJP tower location is inside or outside the plume in the regional model. Hence, we also run another model case with NO mixing ratio values as a function of measured wind direction, based on GEM-MACH NO and wind direction over the same period. In this analysis the GEM-MACH NO values are binned by modeled wind direction in 18 bins (with 20° width) and the median NO value for each bin is calculated in order to capture NO values when GEM-MACH predicted plumes coming from the sources. These median NO values were then used as input for the 1D canopy model based on the measured wind direction at the tower, thus correcting any plume misalignment caused by small errors in GEM-MACH's forecasted wind direction.

In addition to these NO simulations, we also test the 1D model with constant, time-invariant NO mixing ratios. A set of optimization runs demonstrated that the lowest RMS error of ozone mixing ratio was achieved with a constant value of $\text{NO} = 0.05$ ppb. To demonstrate the model sensitivity to NO, we include tests with 0.01 and 0.1 ppb in Section 3.5.

Decaying plant matter can also be a source of NO. Finco et al. (2018) measured NO in a forest near the surface and at 5 heights through the canopy. While the NO between heights of 5 m and 41 m varied from 0.1 to 2.5 ppb in the Finco et al. study, measurements at a height of 0.15 m ranged from 5 to 20 ppb (Finco et al., 2018). Using the parameterization of NO surface emissions from the GEM-MACH model (Williams et al., 1992) with the temperatures over the modeling period suggests that between 0.5 and 1 ppb of NO should be added to the bottom layer of the model during each 30-min time step. While these NO emissions would realistically be diffused upward into the canopy and the profile would depend on

255 turbulence and stability, we approximate these emissions with two case studies where the NO levels in the 3 lowest 1-m model layers are held at either 1 or 5 ppb (with NO = 0.05 ppb for heights above 3 m).

3 Results and Discussion

3.1 Diurnal Ozone Variation by Wind Sector

Figure 3a demonstrates the variation of measured SO₂, CO₂, and sub-micron aerosol total number (*N*) measured at the tower site with wind direction. The SO₂ measurements (reproduced from Gordon et al., 2023) are from two time periods (9-19 June 2018 and 7-25 August 2021). SO₂ is primarily associated with large stack emissions, whereas ozone precursors such as NO_x can also be emitted from vehicles and machinery (e.g. Zhang et al., 2018). Lacking precursor measurements in this study, we rely on SO₂, CO₂, *N*, and the area satellite map to differentiate sectors based on pollutant types. The elevated SO₂ mixing ratios between 160° and 250° demonstrate polluted air being transported to the site, likely from either the Suncor (13.5 km at 195°) or the Syncrude (18 km at 225°) processing facilities. Sub-micron aerosol number (*N*) and CO₂ measurements demonstrate a similar enhancement in the polluted wind sector, but also show enhancement from the north (approximately 0 – 40° for *N* and 340 – 45° for CO₂). Based on these measurements, we very broadly define three wind direction sectors with *polluted* air (i.e. enhanced SO₂, CO₂, and *N*) from 160 – 250°, open *forest* (background SO₂, CO₂, and *N*) from 40 – 160°, and *other* (no enhanced SO₂, but varied industrial sources with some CO₂ and *N* enhancement within the sector) from 250° – 40°. These wind sectors are shown in Figure 1.

While NO and NO₂ were not measured in this study, we can use GEM-MACH output for the period between 1 Jun and 17 Aug as a comparison (Fig. 3b). The GEM-MACH resolution is 2.5 km and the mines and upgrading facilities are more than 10 km (~4 grid squares) from the tower location. Hence, GEM-MACH can resolve these different sectors within at least ± 7°. The GEM-MACH SO₂ output demonstrates a similar pattern to the measurements, with elevated values when winds are from the *polluted* sector, although there are a few elevated values when winds are from the *Forest* and *Other* sectors. In the model output, these represent cases where wind changes in the model result in SO₂ plume directions “looping” so that plumes originating at emissions sources arrive from the other directions. Some emissions from the *other* sector may originate at more distant facility sources between Fort McKay and Bitumount (Fig. 1). Five such cases where GEM-MACH predicted these events arriving from anomalous directions may be seen in Figure 3b. Both NO and NO₂ model outputs demonstrate patterns similar to the CO₂ and *N* measurements, with elevated values when winds are from the *polluted* sector, low values from the *forest* sector, and a mix of low and elevated values from the *other* sector. We note that the delineation between the *forest* and *polluted* sectors (at 160°) is not as clear in the GEM-MACH NO_x output compared to the SO₂ measurement and model output; however, tests demonstrated that moving this line to 145° (for example) had little effect on the results described herein. We also note that the GEM-MACH NO₂ to NO ratios indicate that the NO_x arriving at the site from “forest” and “other” directions is significantly more aged (much higher NO₂ to NO ratios) than NO_x arriving from the

“polluted” direction. This indicates that the NO_x from the polluted direction is relatively fresh, while that from the other directions has experienced more significant photochemical aging.

290 While our companion paper (Jiang et al., 2022) describes source locations for aerosols with finer angular resolution, this is not possible with the ozone measurements since ozone follows a regional diurnal cycle upon which NO titration events are superimposed. There are not enough data to separate both wind direction and time-of-day into more than 3 sectors. Diurnal profiles of ozone measurements separated by the 3 sectors are shown in Figure 4. For ozone measurements made while the generator was operational, measurements from 40 – 60° are removed from the open forest sector (but these angles are included for measurements during solar powered operation). Truncated means (within 3 standard deviations) are shown with shaded areas showing 95% C.I., which demonstrates the significance of the differences between sectors. All sectors show similar temporal patterns. In the summer months ozone mixing ratio is highest in the late afternoon, while in the spring measurements (made 4 times per day), the increase in ozone after sunrise is delayed and ozone mixing ratio is still low near 15:00. The ozone mixing ratio then increases to higher levels near 21:00.

300 Winds are predominantly from the SW in the region, so there are limited data from the *forest* sector, especially for the 1 week of data from Jun 2017. Generally, the ozone mixing ratio was highest when winds were from the *forest* sector, although this is not the case through the afternoon/evening for the longer period 2018 (2 months) measurements, where ozone is lower from the *forest* compared to the *polluted* sector. In 2017 and the longer period (2 months) in 2018, the late afternoon and evening ozone levels when winds are from the *polluted* sector are higher than the *other* (primarily industrial but not forest) sector. The longer period measurements in 2018 (2 months) and 2019 (~3 months) demonstrate elevated overnight ozone levels transported from the *forest* sector relative to the *other* sector, likely representing background air unmodified by oil sands emissions, although these values are not statistically different from the *polluted* sector. These results are similar to previous studies that demonstrate no significant increase in ozone levels with increasing oil sands development (Cho et al., 2017) or ozone levels in the vicinity of oil sands production that are equal to or lower than the background levels (Aggarwal et al., 2018), at these distances from the sources. Although the results shown here are highly variable, there appears to be no significant increase in ozone related to increased air pollution.

310 3.2 Ozone Vertical Profiles

Measurements of ozone mixing ratio and UV radiation within the canopy are shown in Figure 5. These measurements were made on the tower pulley system in the summer 2017 campaign. Ozone tended to increase with height when the UV radiation was also increasing with height, which is the same as the Chen et al. (2018) analysis. This gradient could be due to ozone deposition from stomatal uptake and/or chemical reactions such as near-surface NO_x titration (Chen et al., 2018; Finco et al., 2018). In many profiles, there is a peak of ozone mixing ratio within the canopy near a height of 4 m; however, in many cases, this peak is within the variability of the measurements. Finco et. al (2018) found that the ozone mixing ratio in the mid-level of the forest canopy is about 2.5% higher than the ozone mixing ratio above the canopy. The shading effect (demonstrated by the UV measurements) is in good agreement with the LAI profile (Fig. 2), where the lowest UV values

coincide with the higher LAI value in the lower canopy (between 2 – 8 m), while the shading above 10 m is generally less pronounced.

Longer-term measurements (from 27 March to 23 June 2019) at fixed heights of 2 m and 25 m were used to determine the ozone gradient, as shown in Figure 6. Measurements indicate a stronger gradient overnight (near 0.36 ppb m^{-1}) with a weaker gradient (near 0.18 ppb m^{-1}) in the afternoon. As discussed in Section 2.2, the 95% C.I. for each 15-minute average is 0.24 ppb , which would imply a 95% C.I. in each gradient measurement of 0.02 ppb m^{-1} . Based on the variability in the long-term measurements, the 95% C.I. of each of the 4 mean gradients is $< 0.03 \text{ ppb m}^{-1}$. Hence, all measured gradients are significantly different from zero and the overnight/afternoon difference is significant. A strong gradient would be expected during the night due to increased stability and a greater decoupling of the air above and below the canopy (M17). During the daytime, gradients may be affected by both the decreased photolysis rates within the shaded canopy and the increased turbulence due to afternoon convection. The presence of the canopy may reduce mixing relative to an open space. Continued deposition and/or titration of ozone through the night when there is little mixing will create a stronger gradient as ozone is removed within the canopy. Wu et al. (2016) demonstrate a similar diurnal trend of ozone gradient at a mixed temperate forest in summer with gradients near 0.35 ppb m^{-1} overnight and 0.15 ppb m^{-1} through the day. Our modeling efforts in the following section will attempt to replicate this diurnal variation.

The short-term summertime gradient measurements within the canopy (Fig. 5 and red squares in Fig. 6) are much more variable than the other time periods. The gradients are likely sensitive to short-term variation in ozone mixing ratio during the profiles due to changes in wind direction. These short-term gradients were determined using the difference between the highest measurement and the measurement near a height of 3 m. The near surface measurements were not used for this purpose because of the noted ozone peak near a height of 4 m (Fig. 5). The gradient between heights of near 14 m and near 3 m is therefore considered to be a better representation of the in-canopy ozone gradient. Of the 8 short-term gradient measurements (2017), 3 gradients are very similar to the 2019 long-term spring measured gradients (0.14 to 0.32 ppb m^{-1}), 3 gradients are near zero (although they are within 1 standard deviation of the long-term spring measurements), and 2 of the profiles show strong negative gradients (ozone mixing ratio decreasing with height). Near-zero gradients could be caused by strong mixing. Negative gradients could be due to a change in air-mass above the canopy with a change in winds bringing cleaner ozone-free air (or, alternatively, plumes of NO_x aloft may decrease ozone aloft, resulting in a decrease of ozone with height). The more frequent positive ozone gradients are consistent with surface-based ozone loss, due to deposition and/or surface-based chemical losses.

The ozone vertical profiles measured by the tethered-balloon system in 2018 on three measurement days are shown in Figure 7. The measurement was up to a height of 300 m. Each value shown in the figures is an average over a 20-m interval, and the error bar at each is the standard deviation. The gradient determined from the difference between the highest (300 m) and lowest (20 m) averages ranges from -0.0014 to 0.02 ppb m^{-1} , with an average of $0.0087 \text{ ppb m}^{-1}$.

The average gradient is approximately 20 times smaller than the afternoon gradient observed in the canopy (0.18 ppb m^{-1} shown in Fig. 6). The positive ozone gradient (i.e., increasing ozone mixing ratio with increasing height) suggests ozone loss

at the surface with continued atmospheric mixing. Comparing the three days of ozone mixing ratios to the wind speeds (not shown), lower wind speeds are associated with higher ozone mixing ratios over these 3 days, suggesting production and accumulation in the forest. When the wind speed is higher than 3 m s^{-1} , lower ozone levels are observed suggesting that the increase of wind speed dilutes ozone and decreases the ozone mixing ratio, or there may be insufficient time for ozone production chemistry to occur. Higher wind speeds should also be associated with stronger turbulence, due to enhanced wind shear. The stronger turbulence and mixing could lead to a weaker gradient; however, no correlation between the gradient and the wind speed is seen here.

The nearest regular ozone sonde launches are from Stony Plain, more than 400 km SSW of the YAJP site; however, these launches are rarely done in the afternoon. Between 1986 and 2008, there were 17 launches in the month of June at approximately 17:00 local time (<https://woudc.org/>). The ozone gradients measured by these sondes between heights of 50 m and 300 m ranged from -0.0014 to $0.0307 \text{ ppb m}^{-1}$, with an average of $0.0081 \text{ ppb m}^{-1}$. This average is approximately 7% smaller than our measured gradient average ($0.0087 \text{ ppb m}^{-1}$) over the same height range. By comparison, for the month of July there were 21 launches with an average of $0.0103 \text{ ppb m}^{-1}$, approximately 20% greater than our measured gradient average.

3.3 Modeling Comparison

As discussed in Section 2.4, a series of model configurations were chosen to investigate different physical mechanisms and their effect on the diurnal variation of ozone mixing ratios and the gradients above and within the canopy. The model configurations are listed in Table 1. The model was run for each configuration for the period from 18:00 (local) 20 June to 06:00 (local) 27 July 2018. We disregard the first 12 hours for model spin-up, resulting in 6 days of model output. The first 5 configurations are the variations in input NO discussed in Section 2.4, while the final 5 configurations (#6-10) vary the ozone surface deposition rate and the turbulent mixing. The modeled ozone mixing ratio for each configuration is compared to measured values (both at heights of 22 m) in Figure 8. Statistics (ratio of modeled to observed averages, RMS error, and R^2) for the runs are listed in Table 1. To compare model output and measurements, the 10-min measurements were averaged to 30-min values.

Running the model with a constant NO value (configuration #1) results in an average modeled ozone value equal to the average measured value (Ratio of 1.0) as well as the lowest RMS error (10.7 ppb) of all the configurations. We refer to this configuration as the base case. As discussed in Section 2.4, initial test runs demonstrated miss-alignment of plumes when using the GEM-MACH NO values as input to the 1D canopy model. This is demonstrated by the results of configuration #2, with a relatively high RMS (15.3 ppb) and low R^2 (0.352). Using NO as a function of wind direction (based on GEM-MACH output, but with values corrected according to wind direction) improves the results relative to the GEM-MACH output with an improved RMS (13.8 ppb) and the highest R^2 (0.499). Although using NO as a function of wind direction (#3) improves the correlation relative to the base case (with a constant NO), the model underpredicts the ozone (ratio of 0.88) and the RMS is higher when the NO varies with wind direction (13.8 versus 10.7 ppb). As demonstrated in Figure 8,

using either the GEM-MACH NO or the NO based on wind direction results in complete removal of ozone on most nights, which is not supported by the observations.

Including increased NO near the surface below a height of 3 m (configs. #4 and #5) improves the model performance relative to the base case, with slightly lower ratios (0.98 and 0.91 versus 1.0) and higher R^2 values (0.438 and 0.474 versus 0.423). Very little difference is apparent between the base case and these two configurations in Figure 8; however, modifications of the NO profile are expected to have a more significant effect on the modeled ozone gradients, discussed in the following section.

Removing deposition from the model (config. #6) increases the measurement/model ratio (1.20), increases the RMS error (12.2 ppb), and reduces the R^2 (0.343), while doubling the deposition rate to 0.8 cm s^{-1} (config #8) reduces the ratio (0.91), and increases the R^2 value (0.449) and results in the same RMS error as the base case (10.7). Although diffusion is constrained above the canopy-top by measurements of turbulent kinetic energy (e) and the parameterization of Eq. 1, we also explore the effect of varying the K values by two orders-of-magnitude (especially given that this is anticipated to affect the modeled ozone gradient). For these two configurations, the K values are modified (at all heights) by a factor of 0.5 (config. #9) and a factor of 2 (config. #10), which we designate as weaker (#9) and stronger (#10) mixing, respectively. The weaker mixing results in an improved RMS error (10.2 ppb) relative to the base case (10.7), while stronger mixing increases the RMS error (11.6 ppb). Weakening the mixing results in a model underestimation of ozone (ratio of 0.90) and strengthening the mixing results in a model overprediction (ratio of 1.09). Hence, the results imply that elevated surface NO (accounting for surface NO emissions), stronger ozone deposition, and weaker mixing may give better model performance, but different results are demonstrated by different statistical measures. In the next section, output from these model configurations is compared to measured gradients within and above the canopy.

Except for configurations #2 and 3, most of the model runs follow a similar diurnal pattern (Fig. 8) which reproduces the daily cycle of ozone. However, there are differences between the measured and modeled ozone, most prominently in the mornings of June 22 and 25 and through the day of June 26. The worst aspect of the model behaviour seems to be an underprediction of ozone in the mornings between 06:00 and 12:00, except for the 26th where ozone is overestimated throughout the day and evening (12:00 to 00:00). The 26th was a cloudy day with peak PAR near $900 \mu\text{mol m}^{-2} \text{ s}^{-1}$ (compared to 1300 to 1600 $\mu\text{mol m}^{-2} \text{ s}^{-1}$ for the other days), but this is not translated into lower ozone in the model. The difference on the 26th could be due to elevated NO at the measurement site that is not included in the model due to the assumption of constant NO. The GEM-MACH model (results not shown here) gives elevated ozone and low NO on the 24th, and lower ozone and higher NO on the 26th, which is consistent with this explanation. Observed winds are predominantly from the south on both the 24th and 26th, but wind speeds on the 26th are lower and wind direction is more variable, which could lead to recirculation of emitted pollutants back to the tower location.

3.4 Gradient Comparison

Figure 9 compares the modeled gradients for all model configurations by hour-of-day (averaged for the 6 model days) with the tethersonde measurements (Fig. 9a) and the long-term gradients within the canopy (Fig. 9b). The tethersonde measurements were made between ~11:00 and ~18:00 and range from -0.0014 to 0.02 ppb m^{-1} , with an average of 0.0087 ppb m^{-1} . In this time range (11:00 to 18:00) the modeled gradients above the canopy range from near zero (with either no deposition or stronger mixing, configs. #6 and 10) to 0.024 ppb m^{-1} (with weaker mixing, config. #9). The weaker mixing configuration (#9) gives model results which are closest to the measured values. Both the increased surface NO and the strong depositions configurations (#5 and #8) produce similar diurnal variation of the above-canopy gradients. In the afternoon, these model gradient values are within one standard deviation of 4 of the 8 measured gradient values (6 observed gradients are higher than the modeled values and 2 are lower). The average modeled gradient value for this configuration (0.0066 ppb m^{-1}) is 76% of the average measured value, which can be considered good agreement given the amount of variability in the observations.

Figure 9b demonstrates the average and median hourly gradient between heights of 2 m and 25 m for the 10 model configurations. This can be compared directly to average in-canopy gradient measurements made 4 times daily between 27 March and 22 June 2019. The measured overnight gradient is near 0.35 ppb m^{-1} , while the measured afternoon gradient is near 0.18 ppb m^{-1} . [Although the relative cold in later March and the potential presence of snow might affect the gradients, recalculating the gradients excluding 27 March to 30 April results in an average difference ~1% relative to the complete period.](#) The model was run for a different period (21 – 27 June 2018), since this is when continuous ozone measurements at the canopy top were available. The average temperature in the 27 March to 22 June 2019 period was $8.3^{\circ}C$ compared to $21.0^{\circ}C$ in the 21 – 27 June 2018 period, while the average PAR was similar for the two periods (393 and 401 $\mu\text{mol m}^{-2} \text{s}^{-1}$ respectively). Assuming the two time periods are comparable, the model configurations tend to underestimate the overnight and morning gradients, while estimations of the afternoon and evening gradients are underestimated and overestimated depending on the configuration. All of the model configurations, with the exception of no deposition (#6), demonstrate a diurnal variation which is opposite to the measured pattern. The measurements demonstrate a stronger gradient overnight (as is also seen in the diurnal ozone gradient measurements of Wu et al., 2016 in a mixed temperate forest), while the model generally predicts smaller gradients overnight and higher gradients in the afternoon for nearly all configurations. The only model configurations which are consistently within one standard deviation of the measurements are the weak deposition configuration (#7) with $v_d = 0.2$ cm s^{-1} and the strong mixing (#10), which show good agreement in the afternoon and evening. The weaker mixing configuration (#9) shows good agreement with the overnight and morning gradients but overestimates the afternoon and evening gradients.

[Rannik et al. \(2012\) demonstrate a strong diurnal cycle of deposition velocity, averaging \$0.2\$ \$\text{cm s}^{-1}\$ at night compared to more than \$0.5\$ \$\text{cm s}^{-1}\$ during the day \(in the summer months\). Figure 9b demonstrates that a lower deposition velocity results in a smaller gradient \(compare #6, 7, and 8\). Although our model unrealistically assumes a deposition velocity that is](#)

450 constant with time, the results suggest that modeling a deposition velocity that is lower at night and a higher during the day would result in a weaker gradient at night and a stronger gradient during the day (relative to a constant value). This would further increase the difference between the model results and the observations, which show stronger gradients at night.

Hence, the combined results suggest three possible model corrections: 1) ozone deposition could be weaker in this forest relative to previous studies such as Rannik et al. (2012) and Wu et al. (2016); 2) in-canopy mixing may be overestimated
455 during the night; and 3) in-canopy mixing may be underestimated during the day. We ran various combinations of these 3 modifications (deposition velocity of 0.2 cm s^{-1} , decreased mixing before noon, and increased mixing after noon) and found that using $v_d = 0.2 \text{ cm s}^{-1}$ (#7) combined with a decrease in K by a factor of two between 0:00 and 12:00 (#9 at night only) reproduced the observed pattern of strong gradients overnight and weak gradients through the day (labelled “#7 with #9” in Fig. 9b). All other combinations of the 3 modifications (not shown in Fig. 9b) gave results very similar to other previously
460 discussed configurations and did not reproduce the observed diurnal pattern of the gradients. Hence, these model results suggest that mixing is overestimated overnight, and that deposition velocity is low relative to previous studies. While the mixing is simulated with measured values through Equations 2 and 3, these equations may underestimate the stability at night when fluxes (u_* and $\overline{w'T'}$) are weaker. The deposition velocity may be lower relative to the Rannik et al. (2012) study ($v_d = 0.2 \text{ cm s}^{-1}$ compared to 0.4 cm s^{-1}) due to the lower density of the forest. The LAI of the boreal forest in Rannik et al.
465 ranged from 6 to 8, while the LAI of the mixed temperate forest described in Wu et al. was 4.6, both much higher than the LAI of 1.17 at this site. The estimated deposition may also be affected by the “big leaf” assumption. Spreading the ozone deposition through the vertical profile of the canopy would likely reduce the gradient relative to deposition at the surface only. Hence, the “big leaf” assumption may lead to an overestimation of the deposition rate, further increasing the difference between the model results and the Rannik et al. study.

470 Although, this combined configuration (#7 with #9) is not listed in Table 1 or shown in Fig. 8, the O_3 mixing ratio at a height 22 m with this combined configuration of is similar to that of configuration #7 (weak ozone deposition). The average ratio (modeled to measured ozone) for the combined configuration is 1.05, the RMS error is 10.9 ppb, and the R^2 is 0.402 (compared to 1.07, 11.0 ppb, $R^2 = 0.396$ for config. #7 or 1.00, 10.7 ppb, $R^2 = 0.423$ for the base case #1). Hence, modeling weak deposition with the inclusion of weaker mixing overnight gives a better model performance (for ozone
475 mixing ratio above the canopy) relative to the modeling weak deposition with unmodified mixing; but the performance is slightly worse than the base case with moderate (0.4 cm s^{-1}) deposition and unmodified mixing. However, neither the base case (#1) nor the weak deposition alone (#7) can reproduce the observed diurnal variation of the gradients.

3.5 Additional Sensitivity Analysis

To test the model sensitivity to some of the assumptions, model statistics are generated from modified model runs compared
480 to the base run with $[\text{NO}] = 0.1 \text{ ppb}$ and a surface deposition rate of $v_d = 4 \text{ mm s}^{-1}$ (config. #1). Tests include modifications to the value of the constant NO value, modification of the ozone upper boundary condition (at the highest model level of 1

km), the temperature profile above the canopy (a lapse rate of 0 K m^{-1} is compared to the assumed adiabatic lapse rate of 0.098 K m^{-1} used in the base case), use of a more transparent canopy (with a light extinction coefficient of $k = 0.31$ compared with the base case of $k = 0.68$), the choice of the height z_l used to normalize the canopy diffusion coefficient as
485 $K(z_l)$ ($z_l = 42 \text{ m}$ compared with the base case of $z_l = 23 \text{ m}$), a doubling of the isoprene and monoterpene emissions from the pine trees, and increased LAI (two values of 2 and $3.5 \text{ m}^2 \text{ m}^{-2}$).

Table 2 lists the statistics for the base case and the modified runs. Modeled ozone output at a height of 22 m is compared to measurements from the same height. As discussed in Section 2.4, the model is highly sensitive to the NO input value. The input value of 0.05 ppb was determined through an optimization procedure to minimize the RMS error in the base case. The
490 test results in Table 2 demonstrate that decreasing the NO amount by a factor of 5 (to 0.01 ppb) results in an overestimation of ozone (ratio of 1.45), while decreasing NO by a factor of 2 (0.10 ppb) results in an underestimation of ozone (ratio of 0.84). While decreasing NO lowers the R^2 value relative to the base case, increasing NO results in a higher R^2 value (0.548) due to a stronger diurnal variation in ozone levels.

Lowering the ozone upper boundary condition to 50 ppb reduces the RMS error (to 9.7 from 10.7 ppb) and raised the R^2
495 value (to 0.449 from 0.423), but this causes the model to underpredict the ozone by an average of 13%. Conversely, increasing the upper boundary ozone to 70 ppb results in an overprediction of 12%, increases the RMS error (12.9 ppb), and decreases the R^2 (0.402). Hence there appears to be some sensitivity to this variable with a trade-off between better diurnal variation in the model with less ozone versus an average underprediction relative to the observed average.

Changing the temperature profile above the canopy, the light extinction coefficient, or the height (z_l) that is used to
500 normalize the in-canopy K parameterization (following M17) does not have a significant effect on the statistics, although the R^2 values are slightly higher (ranging from 0.424 to 0.434 for all these cases, compared to 0.423 for the base case). Doubling the basal emission rates of isoprene and monoterpenes or increasing the LAI has no significant effect (<2%) on any of the statistics. We note that a doubled isoprene emission rate corresponds to the warm conifer classification of Guenther et al. (1995) and can hence be considered realistic values. [Changing the model maximum height from 1 km to 500 m results in a](#)
505 [30% average overestimation \(due to the closer proximity of the canopy-top boundary condition to the measurement height\) and a higher RMS error \(15.1 ppb\); however, the \$R^2\$ value is slightly improved \(0.469 from 0.424\). In summary, these results demonstrate that the model is relatively insensitive to the choice of parameter values within the range of values investigated here \(with the exception of input NO mixing ratio\). The sensitivity analyses of this and the previous section suggest that the 1D model results depend most strongly on the assumed NO concentrations and the magnitude of the coefficients of vertical diffusivity \(\$K\$ \). Height dependent observations of both NO and turbulent kinetic energy \(\$e\$ \) as well as
510 \$\text{O}_3\$ are therefore recommended for future studies of this nature.](#)

4 Conclusions

Although there is variability in the results, ozone measurements segmented by wind direction generally support the results of Cho et al. (2017) and Aggarwal et al. (2018), which demonstrate no significant increase in ozone levels (or some ozone reduction) when winds are from the direction of oil sands production relative to background (forested) sources.

In-canopy ozone measurements at heights of 2 m and 25 m indicate a stronger gradient overnight (near 0.35 ppb m⁻¹) with a weaker gradient (near 0.18 ppb m⁻¹) in the afternoon. This is consistent with increased mixing within the canopy in the afternoon (see our companion paper, Jiang et al., 2022) and with the ozone gradient measured in a mixed temperate forest (Wu et al. 2016). Model analysis can reproduce the in-canopy gradients when ozone deposition velocity is modeled as $v_d = 0.2 \text{ cm s}^{-1}$ and the diffusivity coefficients are reduced by a factor of 2 overnight. Model simulations were shown to be most sensitive to the assumed input NO concentration and the coefficient of vertical diffusivity; height-dependent concurrent observations of e , NO, and O₃ are recommended for future work. Ideally, fast ozone (and NO) analyzers could directly measure fluxes (as in Finco et al., 2018) to directly determine deposition velocity and to compare these values to gradient measurements and deposition parameterizations.

The reduced overnight mixing may suggest that modeling nighttime stability using the Obukhov length (Eq. 2) does not account for the increased stability within a canopy associated with canopy decoupling. Moderate overnight canopy decoupling was measured at this site as described in Jiang et al. (2022). Further investigation is needed to improve how this decoupling is incorporated into the 1D canopy model. We note that the parameterization of in-canopy turbulence employed here (M17) imposes a generic shape of observed turbulence profiles below the canopy starting from an above-canopy K value, to attempt to capture this decoupling. However, the local turbulence profile may differ from the generic profile of M17; additional observations of turbulent kinetic energy (e) with height would assist in generating a location-specific K profile for modelling.

Although the deposition velocity resulting in the best fit to observed O₃ profiles is lower here than deposition velocities reported in boreal forests such as Rannik et al. (2012), this could be due to the sparser forest and lower LAI at this location relative to those locations. This lower deposition velocity for ozone contrasts with the higher deposition velocity for SO₂ for this region as described in both Gordon et al. (2022) and Hayden et al. (2022), suggesting that the increased SO₂ deposition could be related to a chemical process such as surface acidity that does not affect ozone deposition. There is also uncertainty associated with the location of the “big leaf” at the forest floor. In future work, the model could be developed to investigate the effect of a vertical distribution of uptake throughout the canopy height.

540 Code/Data Availability

The model code and the field data described in this study will be posted in a data repository prior to publication.

Author Contributions

XZ and MG wrote the original draft of this work and performed the analysis. MG and PM conceptualized the field study. PM acquired funding. XZ, TJ, and MG performed the field experiments. JD provided sonde instrument and instruction tests. 545 DT provided Stony Plain ozonesonde data. XZ, MG, PM, TJ, JD, and DT reviewed and edited the work.

Competing Interests

The contact author has declared that none of the authors has any competing interests.

Acknowledgements

Funding to XZ, MG, and TJ provided by Environment and Climate Change Canada (GCXE20S044). We acknowledge the 550 shared data, technical support, and assistance of the Wood Buffalo Environment Association (WBEA) of Alberta. This research was enabled in part by support provided by the Digital Research Alliance of Canada (alliancecan.ca).

References

- 2B Specifications: <https://twobtech.com/model-205-ozone-monitor.html>, last access: 20 June, 2023.
- Aggarwal, M., Whiteway, J., Seabrook, J., Gray, L., Strawbridge, K., Liu, P., ... McLaren, R: Airborne lidar measurements 555 of aerosol and ozone above the Canadian oil sands region. *Atmos. Meas. Tech.*, 11(6), 3829–3849. doi: 10.5194/amt-11-3829-2018, 2018
- Asthitha, M., Kioutsioukis, I., Fisseha, G. A., Bianconi, R., Bieser, J., Christensen, J. H., Cooper, O. R., Galmarini, S., Hogrefe, C., Im, U., Johnson, B., Liu, P., Nopmongkol, U., Petropavlovskikh, I., Solazzo, E., Tarasick, D. W., and 560 Yarwood, G.: Seasonal ozone vertical profiles over North America using the AQMEII3 group of air quality models: model inter-comparison and stratospheric intrusions, *Atmos. Chem. Phys.*, 18, 13925–13945, <https://doi.org/10.5194/acp-18-13925-2018>, 2018.
- Bocquet, F., D. Helmig, B. A. Van Dam, and C. W. Fairall: Evaluation of the flux gradient technique for measurement of ozone surface fluxes over snowpack at Summit, Greenland, *Atmos. Meas. Tech.*, 4, 2305-2321, doi:10.5194/amt-4-2305-2011, 2011.
- 565 CAPP: Canada's Oil Sands Report. *Canada's Oil and Natural Gas Producers*, 2018.
- Chen, X., Quéléver, L. L., Fung, P. L., Kesti, J., Rissanen, M. P., Bäck, J., Keronen, P., Junninen, H., Petäjä, T., Kerminen, V.-M., and Kulmala, M.: Observations of ozone depletion events in a Finnish boreal forest. *Atmos. Chem. Phys.*, 18(1), 49-63. doi:10.5194/acp-18-49-2018, 2018.

- 570 Cho, S., Vijayaraghavan, K., Spink, D., Cosic, B., Davies, M., and Jung, J.: Assessing the effects of oil sands related ozone precursor emissions on ambient ozone levels in the Alberta oil sands region, Canada. *Atmos. Environ.*, 168, 62-74. doi:10.1016/j.atmosenv.2017.08.062, 2017.
- Clifton, O. E., A. M. Fiore, W. J. Massman, C. B. Baublitz, M. Coyle, L. Emberson, S. Fares, D. K. Farmer, P. Gentine, G. Gerosa, A. B. Guenther, D. Helmig, D. L. Lombardozzi, J. W. Munger, E. G. Patton, S. E. Pusede, D. B. Schwede, S. J. Silva, M. Sorgel, A. L. Steiner, and A. P. K. Tai: Dry Deposition of Ozone Over Land: Processes, Measurement, and
575 Modeling, *Reviews of Geophysics*, 58, doi:10.1029/2019rg000670, 2020.
- Ducker, J. A., Holmes, C. D., Keenan, T. F., Fares, S., Goldstein, A. H., Mammarella, I., . . . Schnell, J.: Synthetic ozone deposition and stomatal uptake at flux tower sites. *Biogeosci.*, 15, 5395–5413, <https://doi.org/10.5194/bg-15-5395-2018>, 2018
- Felzer, B.S., Cronin, T., Reilly, J.M., Melillo, J.M., Wang, X.: Impacts of Ozone on Trees and Crops. *Geosci.*, 339, 784-798,
580 doi:10.1016/j.crte.2007.08.008, 2007.
- Finco, A., Coyle, M., Nemitz, E., Marzuoli, R., Chiesa, M., Loubet, B., Fares, S., Diaz-Pines, E., Gasche, R., and Gerosa, G.: Characterization of ozone deposition to a mixed oak–hornbeam forest – flux measurements at five levels above and inside the canopy and their interactions with nitric oxide. *Atmos. Chem. Phys.*, 18(24), 17945-17961. doi:10.5194/acp-18-17945-2018, 2018.
- 585 Frazer, G.W., Canham, C.D., and Lertzman, K.P.: Gap Light Analyzer (GLA), Version 2.0: Imaging software to extract canopy structure and gap light transmission indices from true-colour fisheye photographs, users manual and program documentation. Copyright © 1999: Simon Fraser University, Burnaby, British Columbia, and the Institute of Ecosystem Studies, Millbrook, New York, 1999.
- Gordon, M., Vlasenko, A., Staebler, R. M., Stroud, C., Makar, P. A., Liggio, J., Li, S.-M. and Brown, S.: Uptake and
590 emission of VOCs near ground level below a mixed forest at Borden, Ontario. *Atmos. Chem. Phys.*, 14(17), 9087-9097. doi:10.5194/acp-14-9087-2014, 2014.
- Gordon, M., Blanchard, D., Jiang, T., Makar, P.A., Staebler, R.M., Aherne, J., Mihele, C., Zhang, X.: High sulphur dioxide deposition velocities measured with the flux/gradient technique in a boreal forest in the Alberta oil sands region. *Atmos. Chem. Phys. Discuss.*, <https://doi.org/10.5194/acp-2022-668>, Submitted 20 Sept 2022.
- 595 Guenther, A.B., Zimmerman, P.R., Harley, P.C., Monson, R.K., and Fall, R.: Isoprene and Monoterpene Emission Rate Variability – Model Evaluations and Sensitivity Analyses, *J. Geophys. Res. Atmos.*, 98(D7), 12 609–12 617, <https://doi.org/10.1029/93jd00527>, 1993.
- Guenther, A., Hewitt, C.N., Erickson, D., Fall, R., Geron, C., Graedel, T., Harley, P., Klinger, L., Lerdau, M., McKay, W. A., Pierce, T., Scholes, B., Steinbrecher, R., Tallamraju, R., Taylor, J., and Zimmerman, P.A.: Global-Model of Natural
600 Volatile Organic-Compound Emissions, *J. Geophys. Res. Atmos.*, 100(D5), 8873–8892, <https://doi:10.1029/94JD0295>, 1995.

- Hayden, K., Li, S.-M., Makar, P., Liggio, J., Moussa, S. G., Akingunola, A., McLaren, R., Staebler, R. M., Darlington, A., O'Brien, J., Zhang, J., Wolde, M., and Zhang, L.: New methodology shows short atmospheric lifetimes of oxidized sulfur and nitrogen due to dry deposition, *Atmos. Chem. Phys.*, 21, 8377–8392, doi:10.5194/acp-21-8377-2021, 2021.
- 605 Jiang, T., Gordon, M., Makar, P.A., Staebler, R., Wheeler, M.: Aerosol deposition to the boreal forest in the vicinity of oil sands, *Atmos. Chem. Phys. Discuss.*, <https://doi.org/10.5194/acp-2022-656>, Submitted 20 Sept 2022.
- Kaplan, W. A., Wofsy, S. C., Keller, M., & Costa, J. M.: Emission of NO and deposition of O₃ in a tropical forest system. *J. Geophys. Res.*, 93(D2), 1389. doi:10.1029/jd093id02p01389, 1988.
- Li, S., Leithead, A., Moussa, S. G., Liggio, J., Moran, M. D., Wang, D., Hayden, K., Darlington, A., Gordon, M., Staebler, R., Makar, P.A., Stroud, C., McLaren, R., Liu, P.S.K., O'Brien, J., Mittermeier, R. Zhang, J., Marson, G., Cober, S.G., 610 Wolde, M., Wentzell, J. J.: Differences between measured and reported volatile organic compound emissions from oil sands facilities in Alberta, Canada. *Proc. Natl. Acad. Sci.*, 114(19). doi:10.1073/pnas.1617862114, 2017.
- Makar, P. A., Fuentes, J. D., Wang, D., Staebler, R. M., and Wiebe, H. A.: Chemical processing of biogenic hydrocarbons within and above a temperate deciduous forest. *J. Geophys. Res.*, 104(D3), 3581–3603. doi: 10.1029/1998JD100065, 1999.
- 615 Makar, P. A., Staebler, R. M., Akingunola, A., Zhang, J., McLinden, C., Kharol, S. K., Pabla, B., Cheung, P., and Zheng, Q.: The effects of forest canopy shading and turbulence on boundary layer ozone. *Nat. Commun.*, 8(1). doi:10.1038/ncomms15243, 2017.
- Mölder, M., Grelle, A., Lindroth, A., and Halldin, S.: Flux-profile relationships over a boreal forest – roughness sublayer corrections, *Ag. For. Meteor.*, 98-99, 645-658, doi:10.1016/S0168-1923(99)00131-8, 1999.
- 620 Morris, G. A., Komhyr, W. D., Hirokawa, J., Flynn, J., Lefer, B., Krotkov, N., and Ngan, F.: A Balloon Sounding Technique for Measuring SO₂ Plumes. *J. Atmos. Ocean. Tech.*, 27, 1318–1330, doi: 10.1175/2010JTECHA1436.1, 2010.
- Natural Resource Canada. (2016, February 19). Oil Sands Extraction and Processing. Retrieved February 03, 2020, from <https://www.nrcan.gc.ca/energy/energy-sources-distribution/crude-oil/oil-sands-extraction-and-processing/18094>
- Pilegaard, K.: Air–Soil Exchange of NO, NO₂ and O₃ in Forests. *Water, Air, Soil Pollut.*, 79–88, 625 <https://doi.org/10.1023/A:1013122230887>, 2001.
- Rannik, Ü., Altimir, N., Mammarella, I., Bäck, J., Rinne, J., Ruuskanen, T. M., Hari, P., Vesala, T., and Kulmala, M.: Ozone deposition into a boreal forest over a decade of observations: evaluating deposition partitioning and driving variables, *Atmos. Chem. Phys.*, 12, 12165–12182, <https://doi.org/10.5194/acp-12-12165-2012>, 2012.
- Smit, H. G. J., Straeter, W., Johnson, B. J., Oltmans, S. J., Davies, J., Tarasick, D. W., Hoegger, B., Stubi, R., Schmidlin, F. 630 J., Northam, T., Thompson, A. M., Witte, J. C., Boyd, I., and Posny, F.: Assessment of the performance of ECC-ozonesondes under quasi-flight conditions in the environmental simulation chamber: Insights from the Juelich Ozone Sonde Intercomparison Experiment (JOSIE), *J. Geophys. Res.-Atmos.*, 112, D19306, doi:10.1029/2006JD007308, 2007.
- Raupach, M.R., Finnigan, J.J. & Brunet, Y. Coherent eddies and turbulence in vegetation canopies. *Boundary-Layer Meteorol.* 78, 351–382, doi:10.1007/BF00120941, 1996.

- 635 Stroud, C.: Role of canopy-scale photochemistry in modifying biogenic-atmosphere exchange of reactive terpene species: Results from the CELTIC field study. *J. Geophys. Res.*, 110(D17). doi: 10.1029/2005jd005775, 2005.
- Williams, E.J., Guenther, A., Fehsenfeld, F.C.: An inventory of nitric oxide emissions from soils in the United States. *J. Geophys. Res.*, 97(D7). doi:10.1029/92JD00412, 1992.
- World Ozone and Ultraviolet Radiation Centre, Government of Canada: <https://woudc.org/>, Last access: 8 November 2022.
- 640 Wu, Z., Staebler, R., Vet., R., Zhang, L.: Dry deposition of O₃ and SO₂ estimated from gradient measurements above a temperate mixed forest. *Environ. Pollut.*, 210, 202-210, <https://doi.org/10.1016/j.envpol.2015.11.052>, 2016.
- Zhang, J., Moran, M. D., Zheng, Q., Makar, P. A., Baratzadeh, P., Marson, G., Liu, P., and Li, S.-M.: Emissions preparation and analysis for multiscale air quality modeling over the Athabasca Oil Sands Region of Alberta, Canada, *Atmos. Chem. Phys.*, 18, 10459–10481, <https://doi.org/10.5194/acp-18-10459-2018>, 2018.
- 645 Zhang, J., Makar, P.A., Kharol, S., Moran, .M.D., and McLinden, C.: An Optimized North America MODIS Leaf Area Index (LAI) Dataset for Air Quality Modeling [Data set]. Zenodo. <https://doi.org/10.5281/zenodo.5393816>, 2021.

650 **Table 1. Model configurations.** NO input and deposition velocity (v_d) are given for each model configuration. When a single NO mixing ratio is given, it is input as constant (in height and time). When two NO mixing ratios are given, the first is for height less than 3 m and the second if for heights above 3 m (both constant in time). Resulting statistics for measured and modeled ozone at a height of 22 m for the 6-day model runs show: ratio of averages (modeled to observed), RMS error, and coefficient of correlation (R^2). The best value in each category is underlined.

| Config. # | NO [ppb] | v_d [cm s ⁻¹] | Description | Ratio | RMS [ppb] | R^2 |
|-----------|-------------|--------------------------------|------------------------------------|-------------|--------------|--------------|
| 1 (base) | 0.05 | 0.4 | Constant NO (with time and height) | <u>1.00</u> | 10.7 | 0.423 |
| 2 | Variable | 0.4 | NO from GEM-MACH | 1.21 | 15.3 | 0.352 |
| 3 | Variable | 0.4 | NO as a function of Wind Dir. | 0.88 | 13.8 | <u>0.499</u> |
| 4 | 0.05, 1 | 0.4 | Elevated surface NO (1 ppb) | 0.98 | 10.7 | 0.438 |
| 5 | 0.05, 5 | 0.4 | Elevated surface NO (5 ppb) | 0.91 | 10.8 | 0.474 |
| 6 | 0.05 | 0 | No ozone deposition | 1.20 | 12.2 | 0.343 |
| 7 | 0.05 | 0.2 | Weak ozone deposition | 1.07 | 11.0 | 0.396 |
| 8 | 0.05 | 0.8 | Strong ozone deposition | 0.91 | 10.7 | 0.449 |
| 9 | 0.05 | 0.4 | Weaker mixing (0.5K) | 0.90 | <u>10.2</u> | 0.420 |
| 10 | 0.05 | 0.4 | Stronger mixing (2K) | 1.09 | 11.6 | 0.417 |

655

660 **Table 2. Model statistics with modified parameters for 2-day model runs.** Ratio of averages (modeled/observed), RMS error, and coefficient of correlation (R^2) are shown. The base case is run with a constant ozone mixing ratio of [NO] = 0.05 ppb, an upper boundary condition [O₃] = 60 ppb at the 1 km model top, a lapse rate of $dT/dz = -9.8$ K km⁻¹ above 29 m, a canopy light extinction coefficient of $k = 0.68$, $z_l = 23$ m, and LAI = 1.17 m. The modeled isoprene and monoterpene emission rates are doubled as a sensitivity test. A model version is tested with a 0.5 km maximum model height. All runs include an ozone surface deposition of $v_d = 4$ mm s⁻¹.

| Model Run | Ratio | RMS [ppb] | R^2 |
|------------------------------------|-------------|--------------|--------------|
| Base case (Config. #2) | 1.00 | 10.7 | 0.423 |
| [NO] = 0.01 ppb | 1.45 | 14.7 | 0.347 |
| [NO] = 0.10 ppb | 0.84 | 11.4 | 0.548 |
| [O ₃] = 50 ppb at 1 km | 0.87 | 9.7 | 0.449 |
| [O ₃] = 70 ppb at 1 km | 1.12 | 12.9 | 0.402 |
| $dT/dz = 0$ for $z > h_c$ | 0.96 | 10.4 | 0.434 |
| $k = 0.31$ | 1.00 | 10.7 | 0.424 |
| $z_l = 42$ m | 0.98 | 10.7 | 0.431 |
| Double iso/mono rates | 0.99 | 10.7 | 0.428 |
| LAI = 2 | 0.99 | 10.7 | 0.426 |
| LAI = 3.5 | 0.98 | 10.8 | 0.428 |
| Model height of 500 m | <u>1.30</u> | <u>15.1</u> | <u>0.459</u> |



Figure 1: The study area and surrounding areas of the measurement sites showing the YAJP tower location (red dot), Syncrude (blue triangle) and Suncor (yellow square) stack locations, and wind sectors (industry, forest, and other) used in the following analysis (based on SO₂, aerosol, and CO₂ measurements). Delineation of the wind sectors is shown by white lines with corresponding wind directions. Map image is © Google Maps.

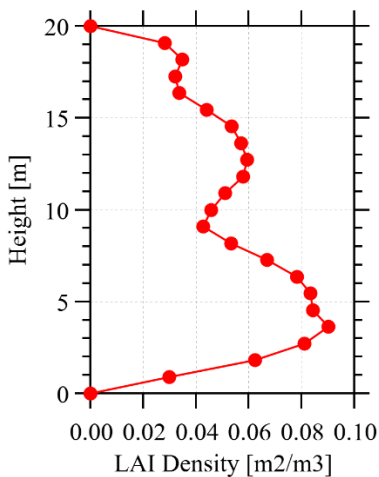


Figure 2: The LAI profile near the YAJP tower.

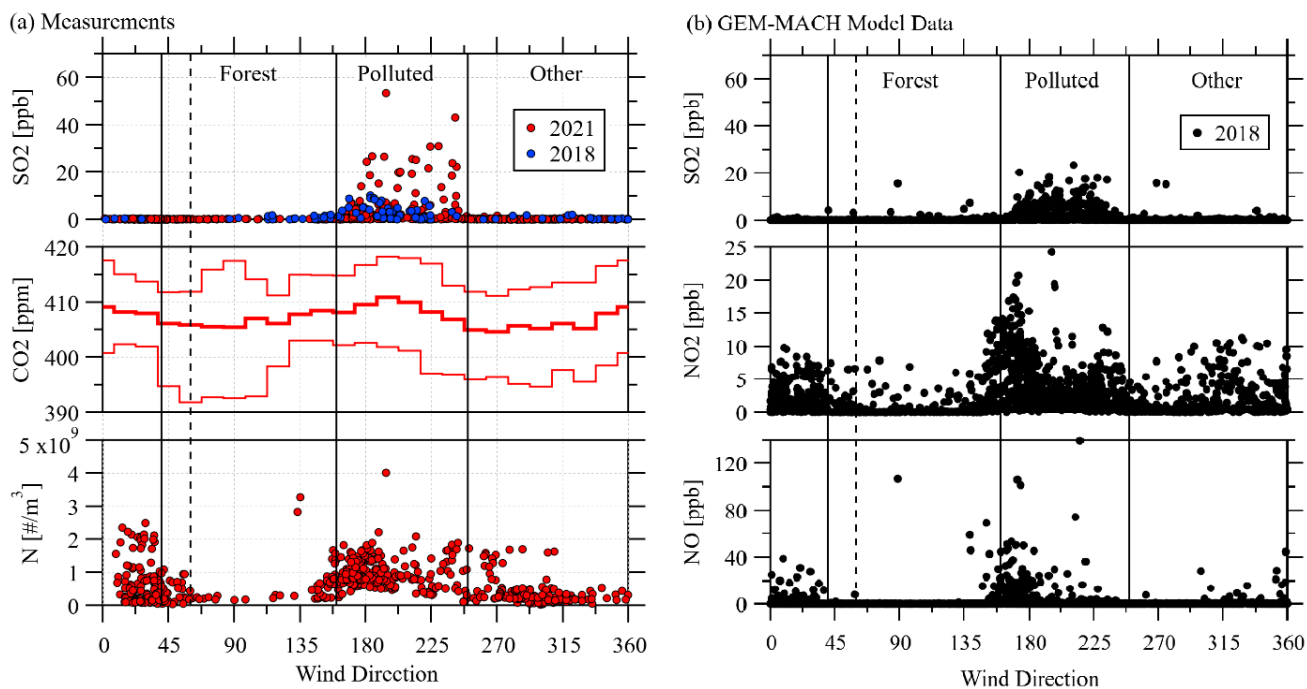
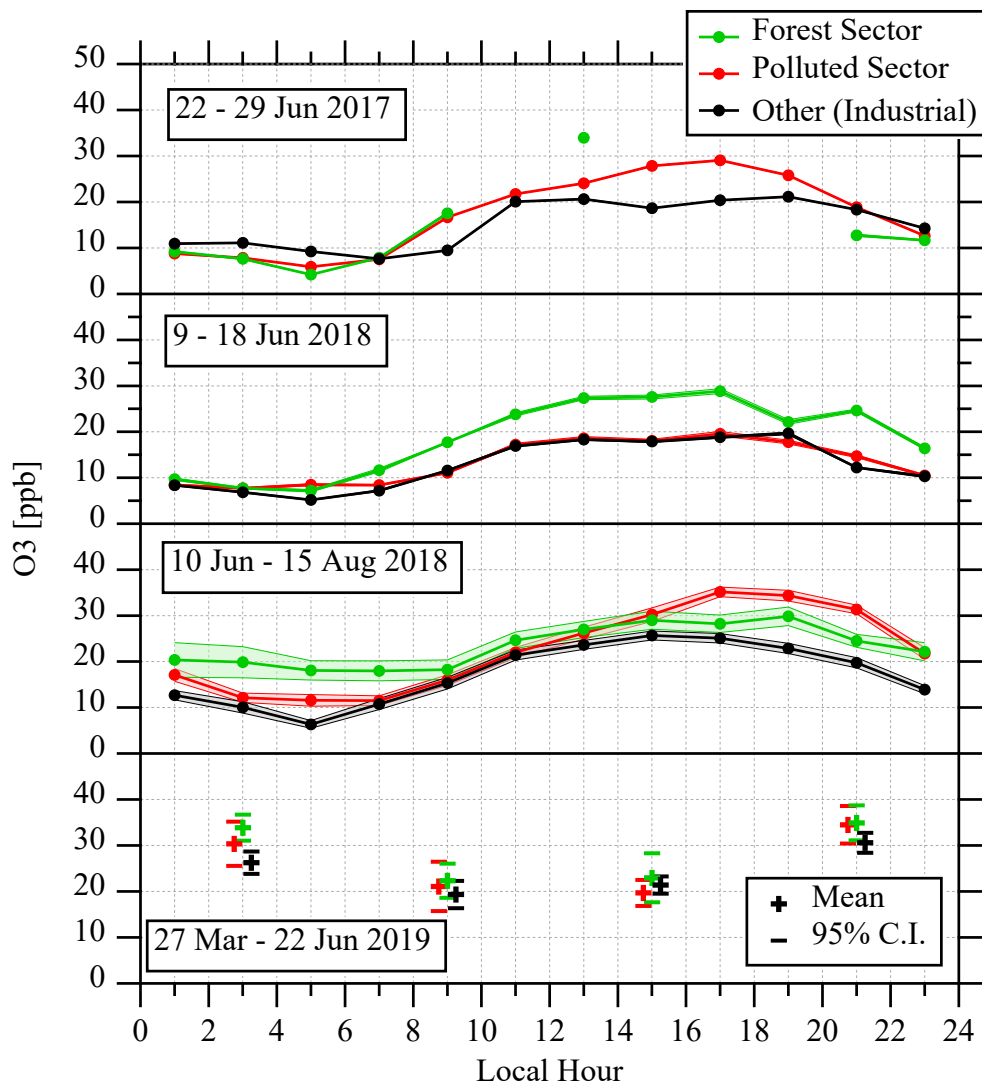


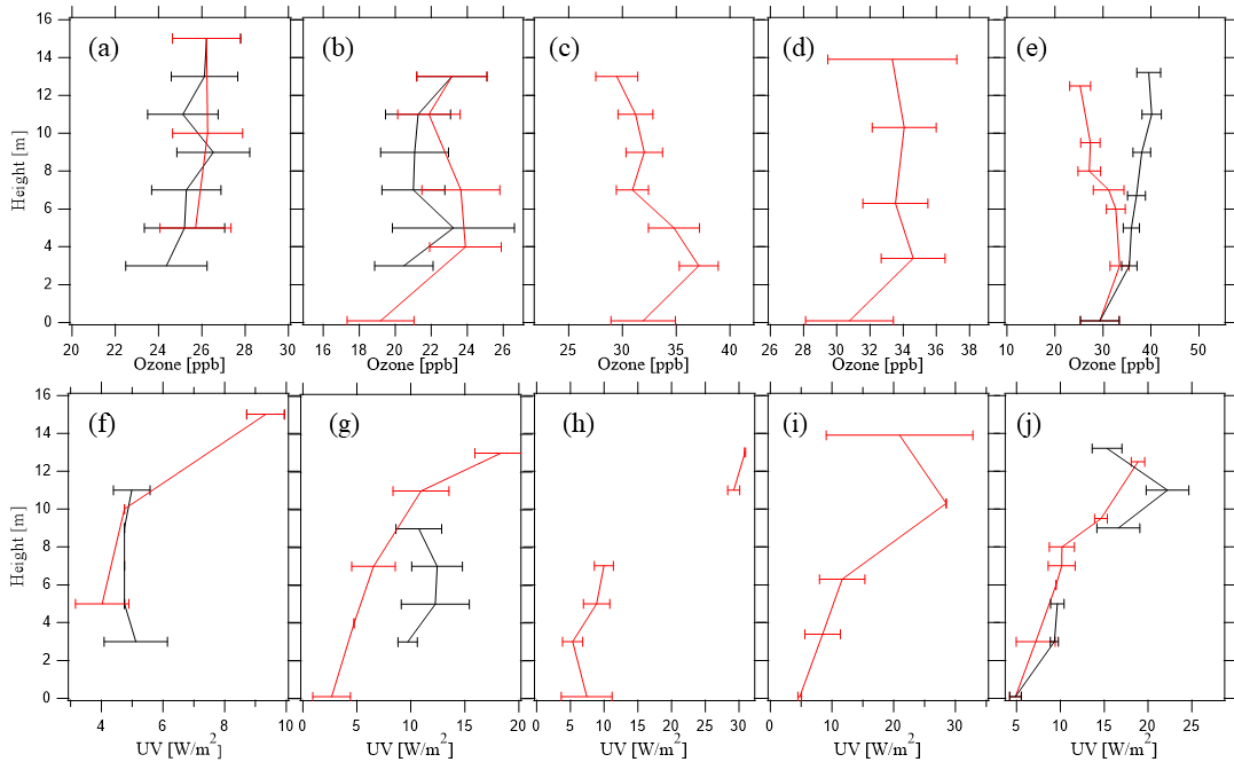
Figure 3: (a) Measured SO_2 , CO_2 , and aerosol number concentration (N) with wind direction ($^\circ\text{N}$). SO_2 measurement from 9-19 Jun 2018 are shown as blue dots. SO_2 and aerosol measurements from 7-25 Aug 2021 are shown as red dots. SO_2 data and aerosol data are reproduced here from the companion papers Gordon et al. (2022) and Jiang et al. (2022). CO_2 mixing ratios were measured from 2017 to 2021 and are shown as median, 25th, and 75th percentiles in 15° bins. (b) GEM-MACH model output of SO_2 , NO , and NO_2 for comparison modeled from 1 Jun to 17 Aug 2018. Vertical lines delineate the 3 sectors used in the analysis (forest, polluted, other) also shown in Fig. 1. The dashed line shows the generator sector ($40 - 60^\circ$). Data in the generator sector are discarded if the generator was used during that period.

675

680



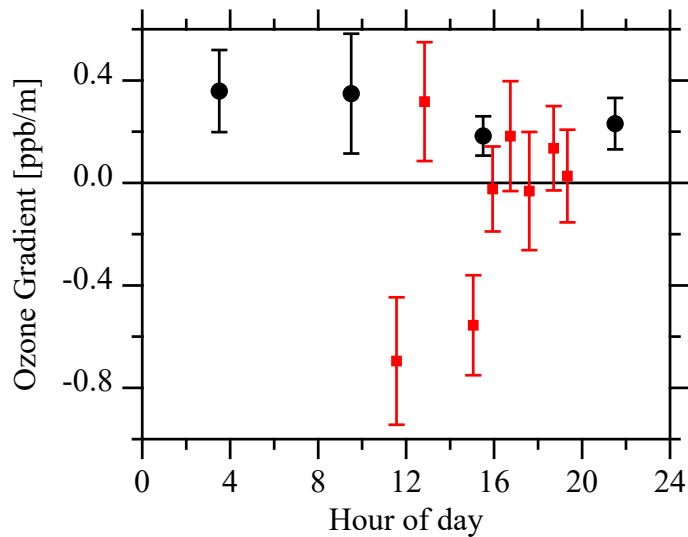
685 **Figure 4: Diurnal cycle of O₃ (truncated mean values in 2-hour bins) from three defined sectors for four measurement periods. Shading shows the 95% confidence interval (shown by error bars for the 2019 data). In 2019, the instruments were run from solar power and were activated only 4 times per day to conserve power. The 2019 sectors are offset at each of the 4 times for ease of comparison, although all measurements were made at the same time. Sectors are defined in the text and are shown in Figs. 1 and 3. Measurement heights were approximately 16 m during 2017, 25 m for 9 - 18 June 2018, 19 m for 10 Jun - 15 Aug 2018, and 25 m for 2019 (the canopy height is approximately 19 m).**



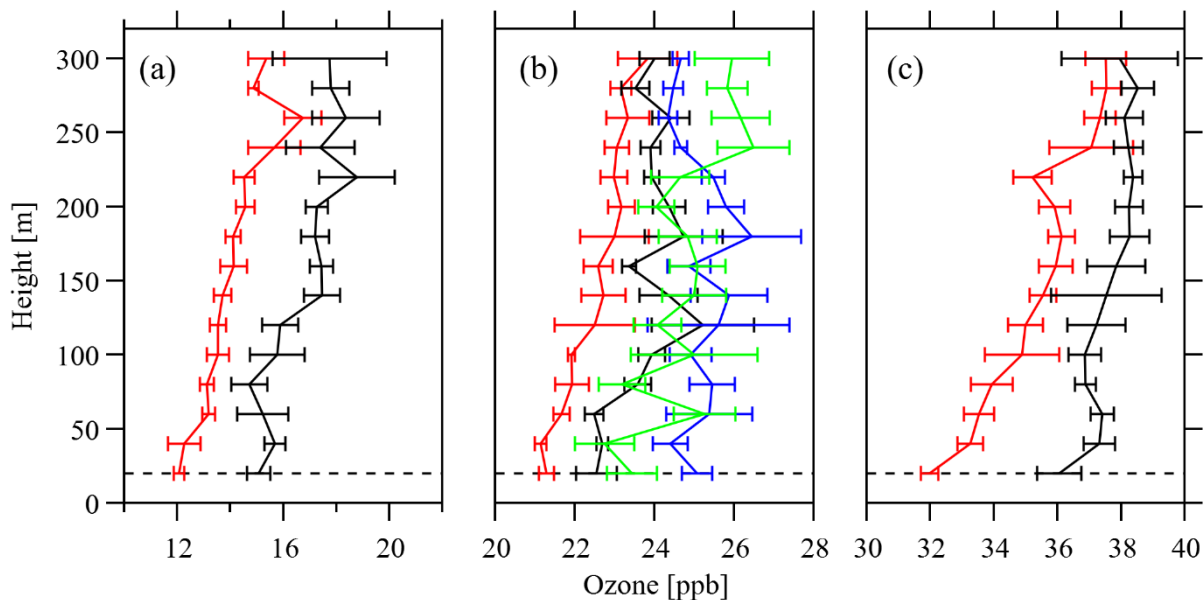
690

Figure 5: Vertical profiles of ozone (a-e) and UV (f-j) from the tower pulley system within the canopy ($h_c = 19$ m). Dates (all 2017) and approximate times are: 18:00, 22 Jul (a,f); 17:00, 24 Jul (b,g); 15:00, 25 Jul (c,h); 15:00 to 18:00, 26 Jul (d,i); 12:00, 27 Jul (e,j). Black lines show ascending measurements, and red lines show descending measurements. Error bars show standard deviations at each height within each 15-min measurement period.

695



700 **Figure 6: Within-canopy ozone gradients as $dC/dz = (C(z_u) - C(z_l))/(z_u - z_l)$. Black circles are gradients between heights of $z_u = 25$ m and $z_l = 2$ m for the period 27 Mar to 23 Jun 2019. Red squares are the average gradients from the 2017 in-canopy profiles shown in Fig. 5 (22 to 27 Jul 2017) with upper height ranging from $z_u = 12.5$ to 15 m and lower height ranging from $z_l = 3$ to 5 m. Error bars show one standard deviation.**



705 **Figure 7: Ozonesonde profiles from above the canopy. Dates (all 2018) and times are (a) 13 Jun 10:45-11:30 (red), 12:30-13:20 (black); (b) 15 Jun 12:00-12:30 (red), 12:40-12:55 (black), 13:05-13:15 (blue), 13:55-14:15 (green); (c) 16 Jun 17:00-17:30 (red), and 17:50-18:00 (black). Error bars show standard deviation in each 20-m height interval. Dashed line shows canopy height ($h_c = 19$ m).**

710

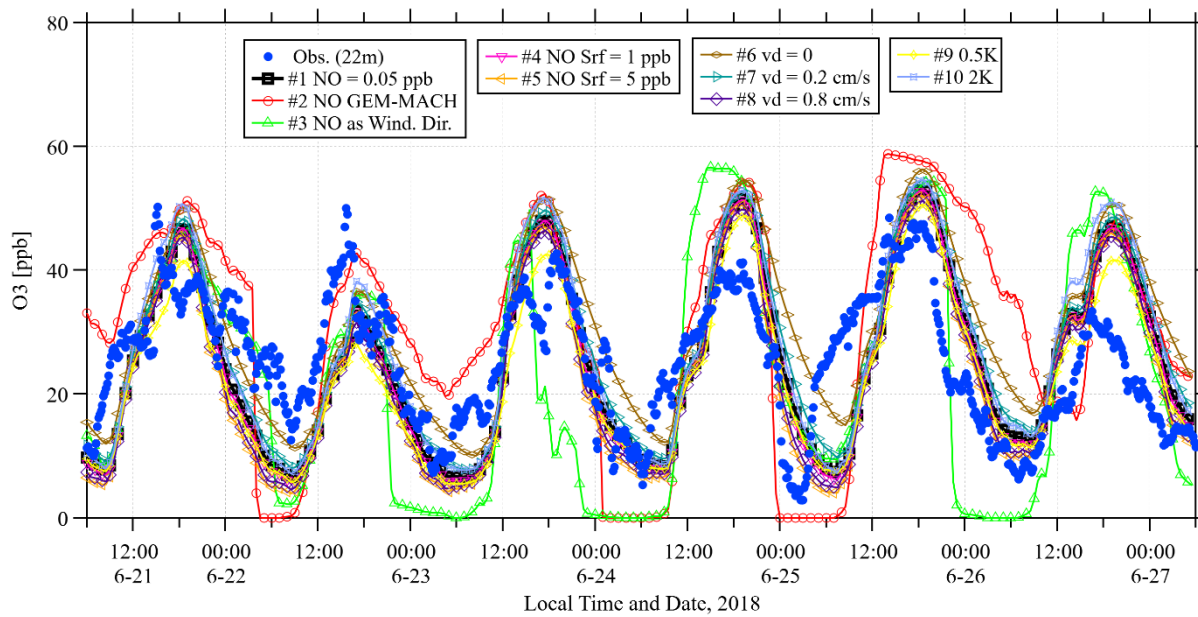


Figure 8: The ozone measurements and model output (at a height of 22 m) for the 10 configurations listed in Table 1. The first 12 hours (not shown) are excluded from the results as model spin-up. Observation frequency is every 10-minues. Model output is 30-min, but only every second marker is shown for clarity.

715

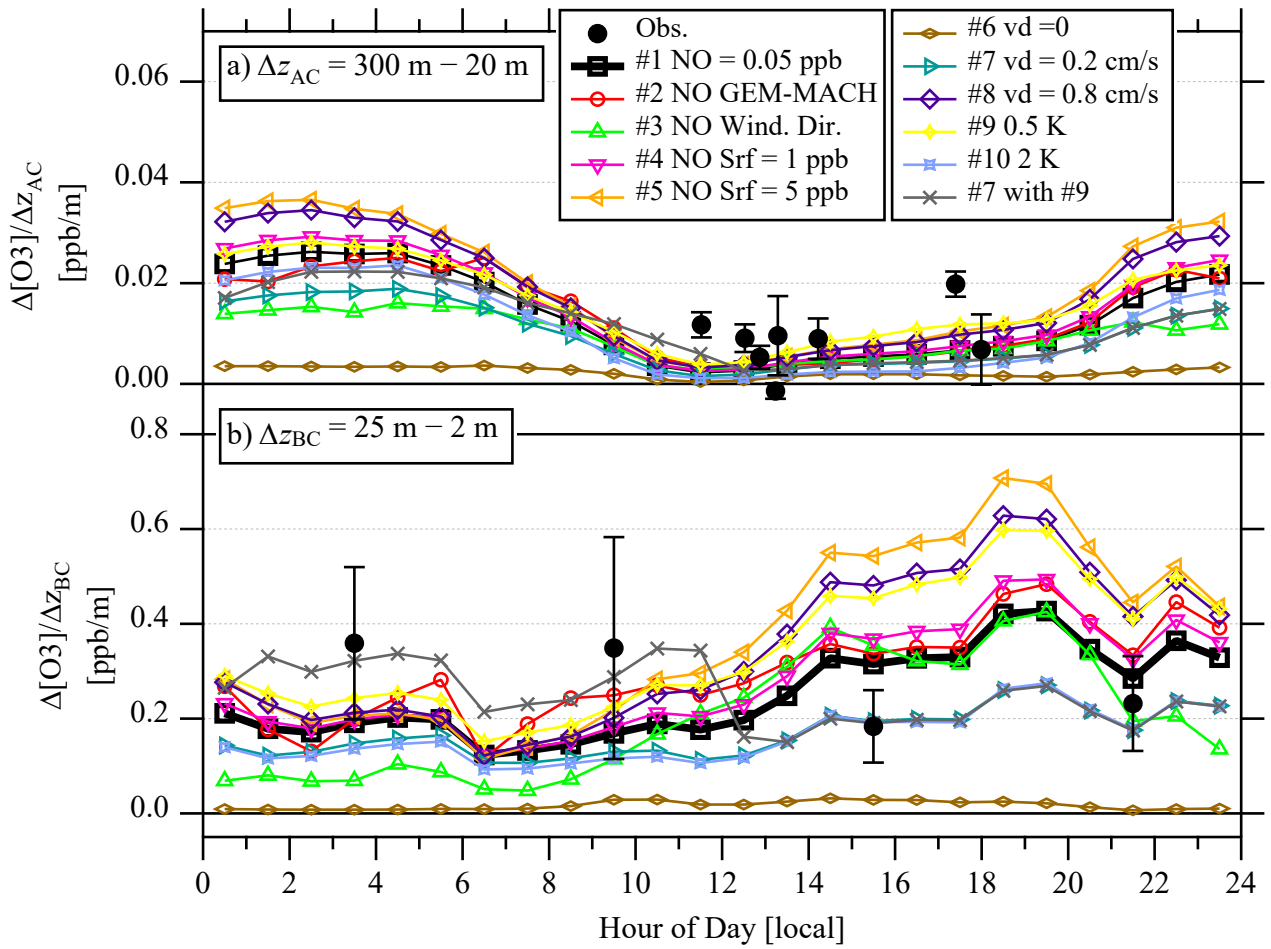


Figure 9: Hourly gradients from the 10 model runs as listed in Table 1. The average ozone gradient is shown (a) above the canopy (AC) between heights of 20 and 300 m and (b) below the canopy (BC) between heights of 2 and 25 m. The black solid circles show measured gradients from the tethered sonde above the canopy (Fig. 7) and the long-term below-canopy gradients (Fig. 6). Error bars show standard deviations of the measurements.

720